

Gap structure and phase diagram of twisted bilayer cuprates from a microscopic perspective

Siddhant Panda,¹ Andreas Kreisel,^{2,3} Laura Fanfarillo,⁴ and P. J. Hirschfeld¹

¹*Department of Physics, University of Florida, Gainesville, Florida 32611, USA*

²*Niels Bohr Institute, University of Copenhagen, DK-2100 Copenhagen, Denmark*

³*Department of Physics and Astronomy, Uppsala University, Box 516, 751 20 Uppsala, Sweden*

⁴*Istituto dei Sistemi Complessi (ISC-CNR), Via dei Taurini 19, I-00185 Rome, Italy*

(Dated: March 12, 2026)

Since the prediction of a time-reversal symmetry breaking (TRSB) $d + id'$ state in twisted bilayer cuprate superconductors by Can et al.[1], several experiments have attempted to detect this state, yielding conflicting results. At present, it is not clear which differences in samples or experimental conditions might explain these discrepancies. In this work, we perform a tight-binding lattice model calculation with phenomenological interlayer tunneling, examining the order parameter as a function of twist angle, interlayer tunneling, doping, and temperature. We observe the TRSB state to be correlated to the position of the Van Hove singularity in the normal state which changes not only as a function of doping but also the tunneling strength. Two such phases are identified as nominally consistent with in-plane $d + id'$ and $d + is$ order, but with unexpected transformation properties under bilayer symmetry operations. We calculate the Josephson critical current, in particular examining the angle dependence for various tunneling strengths. Finally, we discuss the existing experiments in the context of our results.

I. INTRODUCTION

Early theoretical studies of c -axis cuprate Josephson junctions [2, 3] predicted that as one twists two 2D d -wave superconductors from 0° to 45° with respect to each other, the system should undergo a phase transition from a normal superconductor to a time reversal symmetry breaking (TRSB) superconductor with $d + id'$ order parameter. Due to order parameter mismatch between the two monolayers at 45° , first order pair tunneling processes are expected to vanish. Interest in this phenomenon was revived recently by a more thorough theoretical study by Can et al. [1] on 2D twisted cuprates, pointing out the expected existence of topological edge currents in the TRSB state. In addition to Ginzburg Landau calculations, Can et al. employed a continuum model and a microscopic lattice model calculation to solve the superconducting gap equation. In the lattice model for the parameters of their calculation they predicted the TRSB topological state for angles ranging from 37° to 53° .

Since bulk BSCCO-2212 is an extremely 2D system, similar effects are expected in c -axis Josephson experiments on twisted crystals, leading Zhao et al. [4] to prepare new c -axis BSCCO twist junctions to search for signatures of the topological state. In fact, twisted c -axis tunneling experiments have a long history, but they have tended to report mixed results for the angle dependence of the Josephson critical current [5–9], and the differences are not generally understood. Zhao et al. showed in their devices a strong decrease in the critical current as twist angle was increased, with a small but nonzero residual critical current at 45° , which was attributed to second order tunneling processes although the magnitude was larger than expected. Yuan et al. [10] then pointed out that the inhomogeneity in BSCCO could generate an

enhanced second order tunneling with magnitude consistent with the measurements. Other signatures of TRSB behavior reported by Zhao et al. include observing a π -shifted Josephson Fraunhofer pattern as well as half-integer Shapiro steps, although recent studies on twisted cuprate junctions have pointed towards vortices being a possible cause of the observed steps [11].

On the other hand, the predictions for two twisted BSCCO monolayers were arguably more closely approximated in a subsequent experiment using two ultrathin BSCCO flakes on SiO_2/Si twisted with respect to one another [12, 13], rather than crystals. In this experiment the critical current was found to be only weakly dependent on the twist angle, however, with no vanishing or strong depression of the critical current near 45° twist angle, suggesting the absence of the topological state. Possible alternative suggestions for the lack of angle dependence include surface roughness of the substrate on which the exfoliated thin films are placed, variation of tunnel barrier thickness, spontaneous breaking of the fourfold rotational symmetry of the twist junction, and possible impurities in the tunneling barrier introduced in the fabrication process leading to complex tunneling process through the BiO layer[12].

Continuum model calculations defined in the momentum space lack microscopic detail, but have the advantage of accessing all twist angles continuously. The phase diagram for such a model with fixed filling and tunneling strength predicts the existence of a $d + is$ state for all twist angles, and finds the $d + id'$ state only for twist angles close to 45° [14, 15]. The $d + is$ states are stable only far below T_c , and coexist there with the $d + id'$ state near 45° ; however at higher temperatures only the $d + id'$ state is stable[15].

The details of the phase diagram are also sensitive to the form of the tunneling matrix element between layers.

Most models adopt a simple isotropic interlayer hopping, whose magnitude decays exponentially with distance between the pairs of interlayer sites. Calculations have been performed in the $t - J$ model where the interlayer tunneling was modeled by taking the orbital symmetry of the copper and oxygen atoms into consideration [16]. In this approximation, it was observed that the state close to 45° was TRSB but not topological.

The main purpose of this study is to explore the phase diagram of the bilayer system and identify the physical parameters that control the stability of TRSB states. In particular, we aim to understand whether variations in twist angle, filling, or interlayer tunneling can account for the discrepancies between recent critical-current measurements [4, 12] and the variability observed in earlier c-axis twist-junction experiments [5–8]. To this end, we employ a microscopic lattice model, which, while computationally demanding, provides a realistic description of the system and precise control over its parameters. We analyze how tuning the microscopic inputs can drive transitions between TRSB and time-reversal-symmetric (TRS) superconducting instabilities. We do not include disorder, which can induce states near the Fermi level even in the topological phase [17].

It is instructive to examine the full superconducting order parameter, which is a complicated and sometimes counterintuitive object when expressed in terms of sites in the Moiré unit cell. Here we give explicit procedures to project the full self-consistent solution onto allowed irreducible representations (irreps), and to identify the internal phase between those states which condense. We show that the symmetry of the twisted bilayer is D_4 , which has consequences for allowed pairing states with symmetry classes distinct from the standard one-plane TRSB states.

Our conclusions for the phase diagram are very roughly consistent with earlier work [18], but present a much richer picture of the order parameter. Some previous lattice calculations, e.g. Ref. [19], simplify this order by minimizing the free energy within an Ansatz $\Delta = \Delta_{1d} + e^{i\phi}\Delta_{d2}$, i.e. assume d -wave forms in layers 1 and 2 distinguished only by a complex internal phase. Instead, we start with interactions leading to nearest-neighbor bond order parameter, solve self-consistently for the order parameter on every bond, and project onto the given local irrep to determine the symmetry. We further extend the phase diagrams into larger regions of parameter space, where it is possible to see how different twist junctions may induce states with different properties. To help understand why the various TRSB states are stable for different model parameters, we examine the corresponding Fermi surfaces and sublattice spectral functions. Finally, we calculate the critical current for various angles and tunneling strength to access different parts of the phase diagram and provide a possible explanation for the experimental variability in cuprate twist junctions.

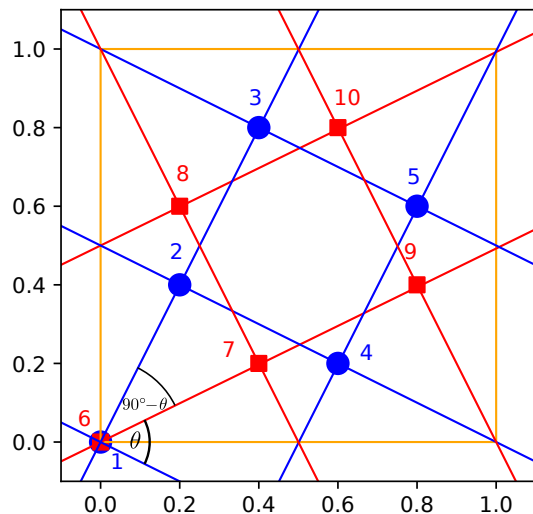


FIG. 1. Supercell for $(m, n) = (1, 2)$ corresponding to twist angle $\theta = 53.13^\circ$. In our manuscript we have written $\theta > 45^\circ$ with the conjugate angle $90^\circ - \theta$ which in this case is 36.87° . Each monolayer has 5 lattice sites twisted by $\theta/2$ in opposite directions. The two monolayers along with the sites and their labels in each monolayer are represented by color blue and red.

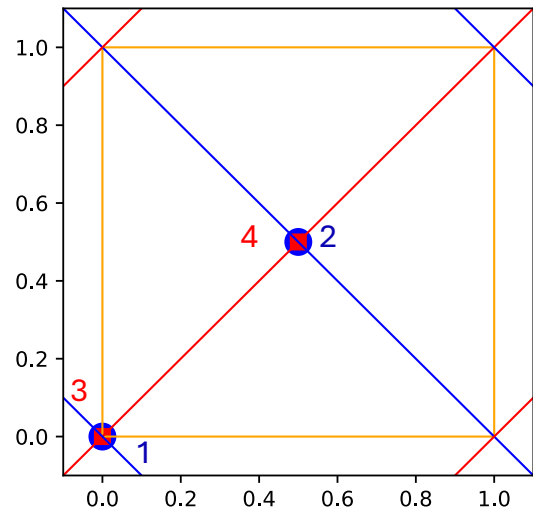


FIG. 2. Supercell for $(m, n) = (1, 1)$ with twist angle $\theta = 90^\circ$. There are four sites in the Moiré unit cell, 2 in each monolayer represented by color blue and red.

II. LATTICE MODEL

In lattice model calculations of Moiré materials we define the model at commensurate angles so as to maintain periodic boundary conditions. These commensurate angles are defined by parameters (m, n) , the twist angle is $\theta = 2 \tan^{-1}(m/n)$ where the two square lattices in our bilayer are twisted by $\theta/2$ in opposite directions. The Moiré unit cell length is $b = \sqrt{m^2 + n^2} \times a$ where a is the single-layer lattice constant and has $2(m^2 + n^2)$ sites, half of which belong to each monolayer, see Fig. 1. For

Irreps	In-plane order parameter	E	$2C_4(z)$	$C_2(z)$	$2C_2'$	$2C_2''$	basis functions (irrep notation)
A_1	s wave	+1	+1	+1	+1	+1	$x^2 + y^2$ (A_1^1), z^2 (A_1^2)
A_2	p wave	+1	+1	+1	-1	-1	z (A_2^1), z^3 (A_2^2), $z(x^2 + y^2)$ (A_2^3)
B_1	$d_{x^2-y^2}$	+1	-1	+1	+1	-1	$x^2 - y^2$ (B_1^1), xyz (B_1^2)
B_2	d_{xy}	+1	-1	+1	-1	+1	xy (B_2^1), $z(x^2 - y^2)$ (B_2^2)
E		+2	0	-2	0	0	(x, y) , (xz, yz) , (xz^2, yz^2) , (xy^2, x^2y) , $(x^3 + y^3)$

TABLE I. Character table for the D_4 group. We project our converged order parameter onto the basis functions of each irrep (notation given in brackets) and the non zero contributions determine the order parameter symmetry. The in-plane order parameters for the different irreps are the s wave, $d_{x^2-y^2}$ wave, d_{xy} wave etc. We refrain from using these labels to identify states in our calculations because they do not contain the full symmetry of the irrep.

the cuprates, a is the Cu-Cu distance in CuO_2 layer.

While we perform our calculations for θ we make use of the C_4 symmetry of the square lattices to rewrite $\theta > 45^\circ$ as $90^\circ - \theta$ such that all the angles in our study range from 0 to 45° to observe the gradual changes in the phase space. We have verified this property by looking at the full phase diagram for 0° ($(m, n) = (0, 1)$) and 90° ($(m, n) = (1, 1)$) and also for 53.13° ($(m, n) = (1, 2)$) and 36.87° ($(m, n) = (1, 3)$) for certain range of parameters.

We solve a two-layer BCS model with nearest neighbor attraction in each layer,

$$H = - \sum_{ij, \sigma d} t_{ij} c_{i\sigma d}^\dagger c_{j\sigma d} - \mu \sum_{i\sigma d} n_{i\sigma d} - \sum_{ij, d} V_{ij} n_{id} n_{jd} - \sum_{ij\sigma} g_{ij} (c_{i\sigma 1}^\dagger c_{j\sigma 2} + h.c.), \quad (1)$$

where i, j are the site indices, $c_{i\sigma d}^\dagger$ and $c_{i\sigma d}$ are electron creation and annihilation operators. $d = 1, 2$ is the monolayer index for the bottom and top monolayer, t_{ij} is the hopping term with nearest-neighbor hopping $t = 0.153$ eV, and next-nearest-neighbor $t' = -0.45t$, consistent with typical cuprate parameters[1]. All energy units throughout this work are in eV. Here μ is the chemical potential which is fixed self consistently to keep the number of electrons (filling) fixed. The band fillings are denoted by ν such that the number of electrons per Moiré unit cell is equal to $2\nu(m^2 + n^2)$. V_{ij} is the nearest-neighbor density-density interaction term factorized in the singlet Cooper channel. We have used $V = 0.2$ eV unless otherwise specified. The layers are coupled by an interlayer tunneling term g_{ij} of the form

$$g_{ij} = g_0 e^{-\frac{(r_{ij}-c)}{\rho}}, \quad (2)$$

where r_{ij} is the total distance between sites i and j in different monolayers. $c = 1$ is the interlayer distance and $\rho = 0.3a$ [1] determines the decay rate of the tunneling. Length scales in this work are denoted in units of $a = 1$. For simplicity, we chose the inter-planar distance equal to the lattice constant which deviates from the real situation in BSSCO bulk crystals. The precise interlayer distances in the fabricated Josephson junctions are not known; furthermore, larger values of c simply scale the value of g_{ij} , such that the qualitative features of the phase diagram are unchanged.

The Hamiltonian in Eq. (1) is redefined in the Moiré basis before we perform our calculations. We relabel $i \rightarrow (\alpha, \mathbf{u})$ and $j \rightarrow (\beta, \mathbf{v})$ where, α, β are the site labels inside a Moiré unit cell and \mathbf{u}, \mathbf{v} are the Moiré unit cell coordinates. We discuss the details of this redefinition along with our algorithm in Appendix A.

Within mean field theory, we solve the superconducting gap equation self consistently,

$$\Delta_{\alpha\beta}(\mathbf{k}) = \sum_{\mathbf{k}'} V^{\mathbf{k}\mathbf{k}'} \langle c_{\alpha\mathbf{k}'\uparrow} c_{\beta-\mathbf{k}'\downarrow} \rangle, \quad (3)$$

where

$$V^{\mathbf{k}\mathbf{k}'} = \sum_{\mathbf{r}} V e^{-i(\mathbf{k}-\mathbf{k}')\cdot\mathbf{r}}, \quad (4)$$

α and β correspond to site labels in our Moiré unit cell, \mathbf{k}, \mathbf{k}' are momenta in the Moiré Brillouin zone and $\mathbf{r} = \mathbf{u} - \mathbf{v}$ is the difference between the nearest neighbor Moiré unit cell coordinates. Examining the symmetry of this cell with arbitrary (commensurate) twist, together with the couplings to its neighbors, allows one to conclude that the symmetry group of the twisted lattice bilayer is D_4 , with character table shown in Table. I. As a concrete example, the cell for a twist angle of 53.13° (36.87°) is shown in Fig. 1. Identifying the symmetry group of the Moiré lattice then allows us to classify the order parameter symmetry of all superconducting states by projecting the converged order parameter onto the D_4 irreps. Using the in-plane basis functions to identify the bilayer order parameters in our calculation does not provide information about the full symmetry of the irrep and hence we denote the order parameter symmetry with the D_4 irrep labels. For example, $A_1 \rightarrow$ “ s ” wave, $B_1 \rightarrow$ “ $d_{x^2-y^2}$ ” wave, $B_2 \rightarrow$ “ d_{xy} ” wave. We describe the procedure in more detail in later sections.

For each α, β , we define the order parameter in the momentum space spanned by the Moiré Brillouin zone. To ensure unbiased convergence of all self-consistency equations, we begin with a random complex initial guess for the order parameter. We then verify that any imaginary component of the converged real-space solution is not an artifact of the initial guess by applying a gauge transformation that maximizes the real part. A true TRSB state is therefore one where the imaginary part of the order parameter in real space cannot be removed

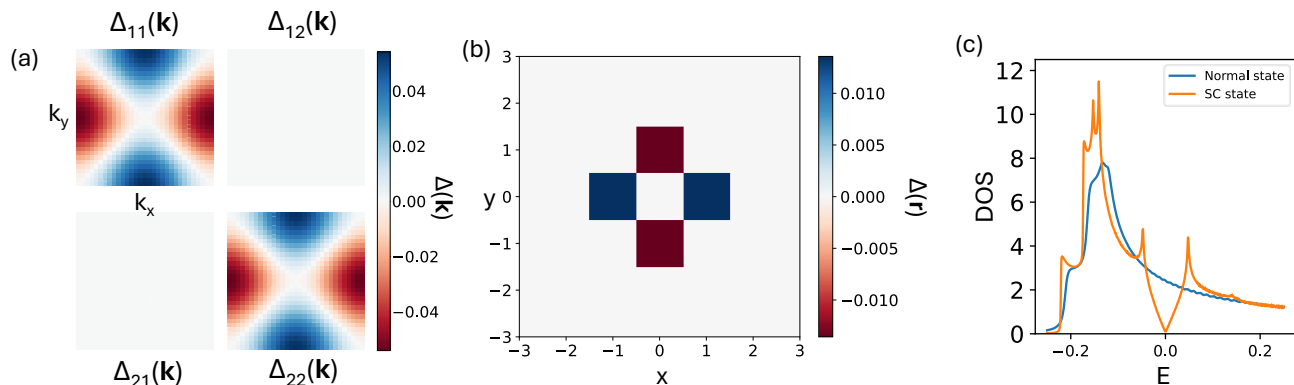


FIG. 3. Order parameter and DOS for $\theta = 0^\circ$ for filling $\nu = 0.49$, interaction strength $V = 0.2$ and tunneling strength $g_0 = 0.01$. (a) B_1 -wave order parameter in momentum space. The 2×2 matrix form of the order parameter is because we have 2 sites in our Moiré unit cell. We clearly see the nodal $d_{x^2-y^2}$ gap along the diagonal elements of the order parameter matrix. (b) d -wave order parameter in real space. The order parameter along the x and y direction have opposite signs. (c) DOS displaying the V-shaped DOS which is a signature of $d_{x^2-y^2}$ order parameter.

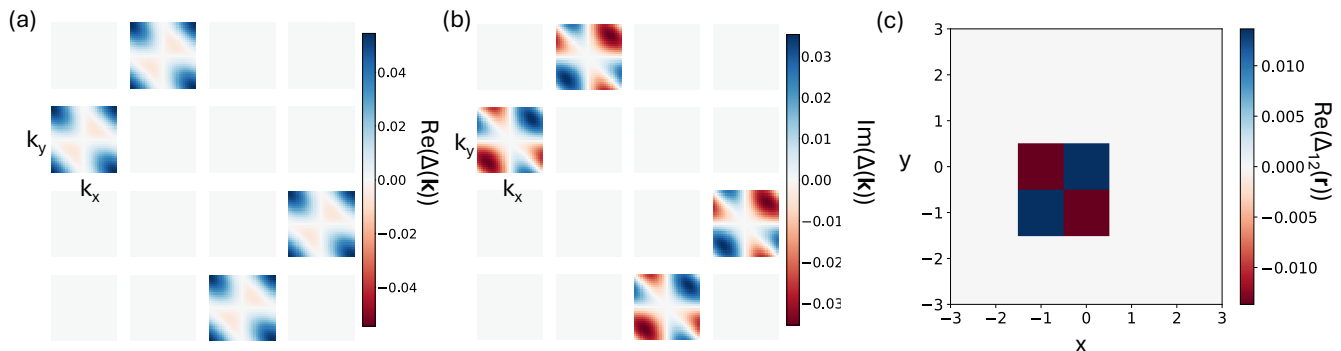


FIG. 4. Real and imaginary part of the order parameter for 90° twist angle for filling $\nu = 0.49$, interaction strength $V = 0.2$ and tunneling strength $g_0 = 0.01$. This system has 4 sites in each Moiré unit cell (Fig. 2) and hence we have a 4×4 order parameter matrix. With two sites in each monolayer the nearest neighbor of site 1 is site 2 and hence we only have off-diagonal elements. (a) Real part of the order parameter and (b) imaginary part of the order parameter have the same form as had been derived in Eq. (5). (c) The real space order parameter is purely real with non zero entries corresponding to Moiré unit cell coordinates of the nearest neighbors. All momentum labels are in units of the Moiré unit cell lattice constant b .

by such a gauge transformation and stays nonzero at the end of this procedure.

When the gap equations have converged, depending on the commensurate angle (m, n) , our order parameter will then be a $2(m^2 + n^2) \times 2(m^2 + n^2)$ matrix. The order parameter $\Delta_{\alpha\beta}(\mathbf{k})$ connecting different layers remains zero since Eq. (1) contains only in-plane interactions V_{ij} , while the Fourier transformed pair amplitudes $\langle c_{\alpha\mathbf{k}\uparrow} c_{-\beta\mathbf{k}\downarrow} \rangle$ are nonzero. Furthermore, since we only have nearest neighbor interactions, we expect non-zero order parameter only where (α, u) and (β, v) are nearest neighbors.

III. ORDER PARAMETERS FOR DIFFERENT TWIST ANGLES.

Before we scan the full phase space as a function of twist angle (θ) , filling (ν) and tunneling strength (g_0) ,

we illustrate how the order parameter appears for some special limiting cases. For 0° twist angle but arbitrary tunneling strength, the model Eq. (1) has been explored earlier in the singlet channel, and is known to exhibit not only d -wave pairing, but also s or $s + id$ depending on g_0 and ν [20]. Since each monolayer is tetragonal, the 90° twist angle is physically equivalent to 0° ; hence we expect the same state for the same Hamiltonian parameters. The key difference between the representations of the order parameters at 0° and 90° arises from the different number of sites in the corresponding Moiré unit cell, leading to different dimension of the order parameter matrix. The matrices are physically equivalent but visually different. We first examine a $B_1(d_{x^2-y^2})$ wave state for 0° and the physically equivalent 90° twist angle to illustrate the Moiré representation in some detail, and then consider nontrivial twist cases with these features in mind.

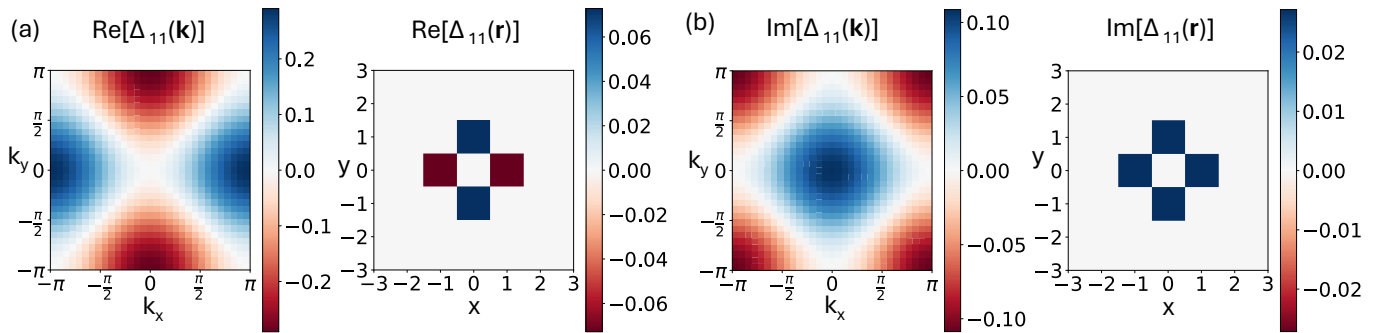


FIG. 5. Real and imaginary part of Δ_{11} both in momentum and real space for 0° twist angle and filling $\nu = 0.4$, tunneling strength $g_0 = 0.05$ and interaction strength $V = 0.5$. (a) Real part of order parameter in momentum and real space. We observe d wave state. (b) We have a extended s wave order parameter in momentum and real space and a non zero imaginary component in real space even after performing the gauge transformation.

A. 0° twist angle

The 0° twist angle is defined by $(m, n) = (0, 1)$, and the order parameter is a 2×2 matrix for each momentum point in the Moiré Brillouin zone. Since at $g_0 = 0$ and near half-filling we have two decoupled, untwisted layers, we expect for weak coupling of these planes to obtain a stable B_1 wave state. In Fig. 3(a), we plot for filling $\nu = 0.49$, $g_0 = 0.01$ the full momentum dependence of the order parameter matrix for each bond i, j . Indeed we observe a nodal B_1 wave order parameter along the diagonals ($\Delta_{11}(\mathbf{k})$ and $\Delta_{22}(\mathbf{k})$), but since the model includes no interlayer pairing term, we find $\Delta_{12}(\mathbf{k}) = \Delta_{21}(\mathbf{k}) = 0$.

Fourier transforming the converged order parameter from momentum to real space, we observe in Fig. 3(b) the expected nearest neighbor $d_{x^2-y^2}$ pairing amplitudes with opposite signs on x and y bonds, as well as the usual V-shaped density of states (DOS) characteristic of d wave superconductors Fig. 3(c).

B. 90° twist angle

The 90° twist angle corresponds to $(m, n) = (1, 1)$ with a 4×4 order parameter matrix for each momentum point in the Moiré Brillouin zone. For the same set of parameters as for 0° , the order parameter converges to a B_1 wave order parameter, shown in Fig. 4, which appears rather different from the 0° case, although it must be physically equivalent. We have 2 sites per monolayer in our Moiré unit cell (Fig. 2), such that the analytical solution for the order parameter between sites 1 and 2 for our case of a nearest neighbor pairing interaction is given by

$$\Delta_{12}(\mathbf{k}) = \Delta_{12}[(1 + \cos(k_x + k_y) - \cos(k_x) - \cos(k_y)) + i(\sin(k_x + k_y) - \sin(k_x) - \sin(k_y))]. \quad (5)$$

The non-zero imaginary part of the order parameter is due to working with the Hamiltonian in the Moiré unit

cell basis. We have performed the full derivation in the Appendix B.

As seen in Fig. 2, the nearest neighbor of site 1 is site 2 in each Moiré unit cell. The Moiré unit cells with coordinates $(0, -1)$, $(-1, 0)$ and $(-1, -1)$ (in units of the Moiré lattice constant b) with respect to the $(0, 0)$ cell shown in Fig. 2 enter the Fourier transform, but are not symmetric about $(0, 0)$, and hence we obtain a non zero imaginary part of the order parameter.

The results after the self consistency are presented in Fig. 4. The real part of the order parameter in Fig. 4(a) is apparently different from the B_1 wave order parameter we obtained in Fig. 3(a), but follows the analytical form we presented in Eq. (5) and plotted in Fig. A3 in the appendix. $\Delta_{12}(\mathbf{k}) = \Delta_{21}^*(\mathbf{k}) = \Delta_{34}(\mathbf{k}) = \Delta_{43}^*(\mathbf{k})$ are the non zero entries because 1, 2 and 3, 4 are nearest neighbors of each other and lie in the same monolayer; all other entries are zero. The imaginary part of $\Delta_{12}(\mathbf{k})$, shown in Fig. 4(b), is not due to having a complex initial guess and cannot be gauged away.

On performing the Fourier transform, we obtain the real part of the order parameter in real space (Fig. 4(c)) which seems to be different from Fig. 3(b) but is equivalent. This can be understood by realizing that the non zero entries correspond to the nearest neighbor Moiré unit cell coordinates as noted above. The imaginary part of the order parameter in real space is 0 and hence we have a pure B_1 wave solution as expected.

C. Observing time reversal symmetry breaking states for 0° twist angle.

Thus far, we have discussed a B_1 wave solution for 0° twist and weak interlayer tunneling. As we vary the interlayer tunneling g_0 and the filling ν we observe TRSB states, e.g. at $\nu = 0.4$, $g_0 = 0.05$ and interaction $V = 0.5$ shown in Fig. 5. We have chosen a larger value of V to obtain a larger superconducting gap in order to observe and benchmark features of the TRSB states. We use more realistic values for our phase space scan. The real

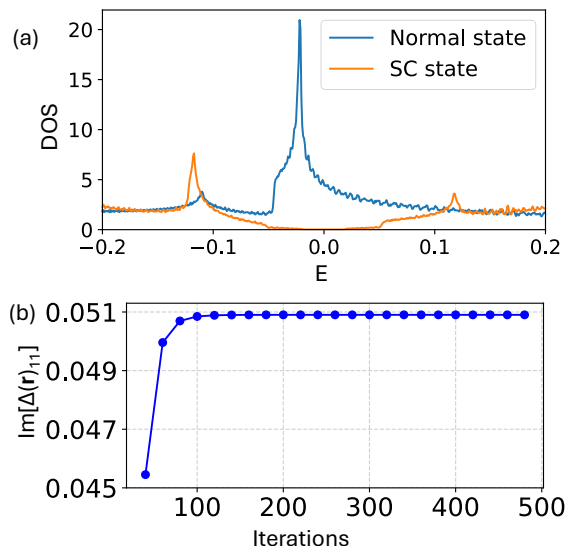


FIG. 6. Signatures of time reversal symmetry breaking for $\theta = 0^\circ$ twist angle case discussed in Fig. 5(a) Gapped DOS observed in the SC state along with the coherence peaks and Van Hove singularity peaks. (b) Imaginary part of the order parameter in real space for the 11 matrix element vs no of iterations. The convergence of this quantity to a finite non zero value indicates the presence of a TRSB state.

part of the order parameter in momentum and real space is B_1 wave state as shown in Fig. 5(a); the imaginary part of the order parameter in momentum space has A_1 -wave behavior as shown in Fig. 5(b). On performing Fourier transform, we find a non-zero imaginary part of the order parameter in real space which cannot be gauged away. Thus we obtain a $B_1 + iA_1$ wave state. This state at nonzero tunneling but zero twist angle is related to the well-known $d_{x^2-y^2} + is$ state found in a somewhat different filling range at $g_0 \rightarrow 0$ [20].

A key difference between a TRS B_1 wave state and a fully gapped TRSB $B_1 + iA_1$ or $B_1 + iB_2$ state is the DOS, since any nodes are lifted by the out-of-phase component. We plotted the DOS of the normal and SC state in Fig. 6(a). Compared to the normal state DOS we can see the gap opening along with the coherence peaks and shifted Van Hove peaks. Calculating the DOS with sufficient resolution to distinguish TRSB states from TRS states is computationally challenging since the Moiré unit cell grows as we approach the 45° twist. Hence, we examined signatures of TRSB that could be obtained directly from the order parameter.

We investigate the imaginary part of the real space order parameter to differentiate between TRS and TRSB states. For $\theta = 90^\circ$ we discussed a B_1 wave state with complex momentum space order parameter which after the Fourier and gauge transform was purely real in real space. In contrast, in Fig. 6(b) we exhibit the imaginary part of the real space order parameter as a function of iterations and its convergence to a nonzero value after gauge transformation, a signature of a TRSB state.

The continuum model calculation predicted regions of $d + is$ order at low temperatures for small twist angles, and coexisting $d + is$ and $d + id$ phases for angles close to 45° [14]. Neither a gapped DOS nor a finite imaginary part of the order parameter in real space provide us with any information about the order parameter symmetry here. Looking at the order parameter momentum dependence ($\Delta(\mathbf{k})$) to identify the symmetry is also challenging for θ close to 45° because of the complicated order parameter matrix. However, the exact symmetry of the order parameter is directly obtainable by Fourier transforming $\Delta_{\alpha\beta}(\mathbf{k})$ to $\Delta_{\alpha\beta}(\mathbf{r})$ and projecting it onto each irrep basis function of the D_4 group. We use the coordinates of the center of each bond during projection, translating bonds which lie outside the Moiré unit cell by the Moiré unit cell lattice vectors into the elementary cell. The nonzero components after projection identify the order parameter symmetry. We only project the order parameter onto a few low order basis functions for each irrep and not all harmonics, hence the magnitude of the order parameter for each irrep (Δ^Γ) is not properly normalized and is reported below in arbitrary units (a.u.).

D. 36.87° twist angle.

The 36.87° twist angle is the conjugate of 53.13° defined by $(m, n) = (1, 2)$. The order parameter is a 10×10 matrix for each \mathbf{k} point. Using the parameters $\nu = 0.4$ and $g_0 = 0.12$, we converged to a $B_1 + iA_1$ state which is shown in Fig. 7

The momentum dependence of each matrix element $\Delta_{ij}(\mathbf{k})$ is dependent on the Moiré unit cell coordinates of the nearest neighbor. For example, $\Delta_{13}(\mathbf{k})$ has a momentum dependence along the y direction because the nearest neighbour bond between site 1 and site 3 connects Moiré unit cells with coordinates $(0, 0)$ and $(0, -1)$. Similarly for Δ_{14} the bond is along $(-1, 0)$ and for Δ_{15} the bond is along $(-1, -1)$ and hence the corresponding momentum dependence is along x axis and the diagonal respectively.

To determine whether the state is TRSB or not, we evaluated the DOS and observed the gap shown in Fig. 8. The occurrence of a gapped $B_1 + iA_1$ state for twist angles close to 45° can therefore provide an explanation for significant Josephson currents for twist angles close to 45° [12]. Since other gapped states are also possible within the same model, we explore other parameter ranges to ascertain which gapped ground states are plausible.

IV. PHASE DIAGRAM

The observation of a $B_1 + iA_1$ state at 36.87° where $B_1 + iB_2$ was predicted earlier[1] (at smaller g_0) already hints at a transition from one TRSB state to another. Clearly we would like to identify all possible TRSB phases (identified in Fig. 9 by shaded regions), and any other fully gapped phases. In this section, we there-

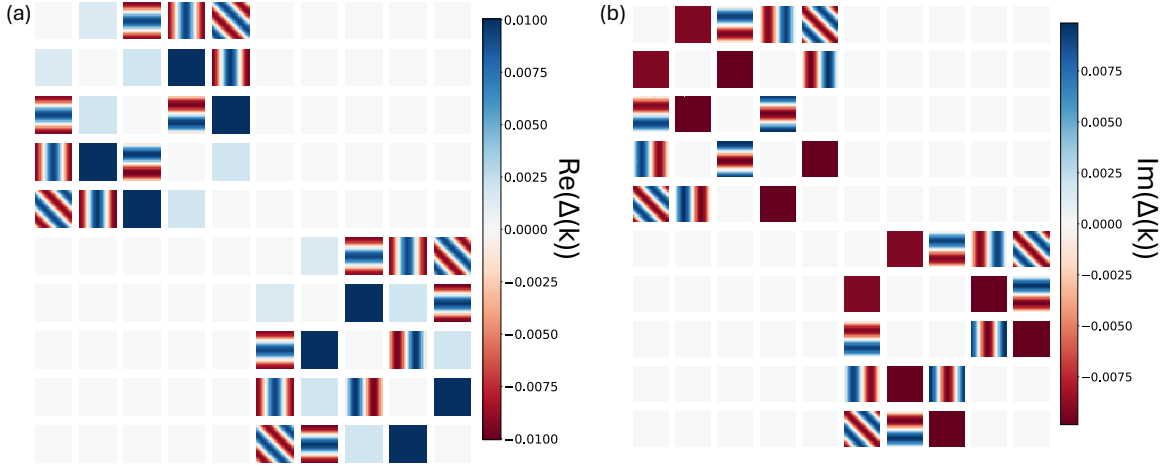


FIG. 7. Order parameter for 36.87° twist angle, filling $\nu = 0.4$, tunneling strength $g_0 = 0.12$, interaction strength $V = 0.2$. There are 10 sites in our Moiré unit cell (Fig. 1) and thus we have a 10×10 matrix. (a) Real part of the order parameter. (b) Imaginary part of the order parameter.

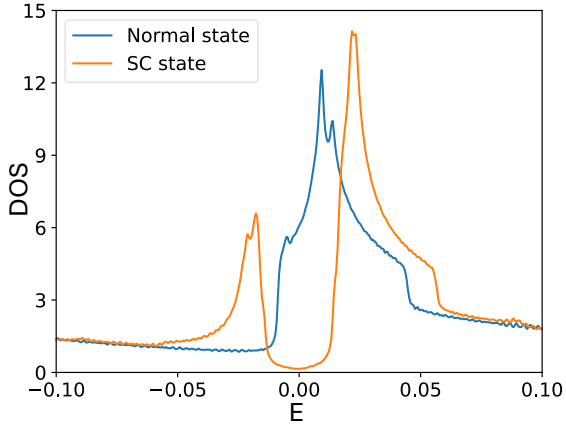


FIG. 8. DOS for $\theta = 53.13^\circ$, filling $\nu = 0.4$, tunneling strength $g_0 = 0.12$ and interaction strength $V = 0.2$ case along with the normal state DOS. We observe the gap opening which is a signature of the TRSB state.

fore discuss the $\nu - g_0$ phase diagram, shown in Fig. 9, for various commensurate angles θ at temperature $T = 10^{-4} \ll \Delta$. We first describe the phases observed at the various angles considered, and subsequently advance some ideas why these phases exist and why certain transitions occur.

For the model given by Eq. (1) on a single layer square lattice, as one dopes away from half filling to lower fillings, the d wave ground state gives way to a $d + is$ phase and eventually to a s wave state[21, 22]. For $\theta = 0^\circ$ and $g_0 = 0$, the two monolayers in our model are decoupled and hence we expect to see similar feature in our phase diagram. As seen in Fig. 9, a pure B_1 wave state spans the filling range $\nu \in [0.49, 0.35]$, $B_1 + iA_1$ state spans $\nu \in [0.35, 0.1]$ and the A_1 wave state is stable for $\nu \in [0.1, 0.05]$. Thus the search for TRSB states begins already with the decoupled untwisted bilayer $B_1 + iA_1$

state, which is also stabilized at fillings closer to half-filling as g_0 increases.

At 28.08° twist angle, we perform the phase space scan for $\nu \in [0.3, 0.49]$. On increasing g_0 we move from a green region of $B_1 + iB_2$ wave states to a blue region of $B_1 + iA_1$ wave states separated by a narrow region of B_1 wave states which are also present for large g_0 . The phase diagram for 36.87° is qualitatively similar to 28.08° . We performed the scan for $\nu \in [0.35, 0.49]$. We observe that the area of the $B_1 + iB_2$ state is significantly larger and persists up to higher tunneling strengths and the region of TRS B_2 wave state separating $B_1 + iB_2$ and $B_2 + iA_1$ phase is significantly reduced. The closest angle to 45° for which we performed calculations was 43.60° for $\nu \in [0.4 - 0.49]$. The area of $B_1 + iB_2$ state has further increased. The region of B_2 wave state separating the $B_1 + iB_2$ and $B_2 + iA_1$ has vanished and instead we have coexistence region where both $B_1 + iB_2$ and $B_2 + iA_1$ state exist. We have explicitly shown the evolution of the projected order parameters for various θ in Appendix C.

We note that the various possible ground states found are expected to be very close in energy as the Fermi surface becomes more complicated at high twist angles. Performing self consistent microscopic calculations can become computationally expensive as we approach twist angles closer to 45° , and with our current momentum grids (31×31 for $\theta = 36.87^\circ$ and 13×13 for $\theta = 43.6^\circ$), eigenvalue crossings with g_0 or ν are not always resolved accurately. One possible such example is for $\theta = 28.08^\circ$, we observed some isolated $B_1 + iB_2$ solutions for $\nu = 0.47$, $g_0 = 0.05$ immersed in regions where B_1 or $B_1 + iB_2$ states appear to be dominant.

Understanding the stability of the various phases found requires a knowledge of the position of the Van Hove singularity in the model relative to the Fermi level, as well as the strength of the pairing interaction evaluated on nested regions of the Fermi surface. We begin

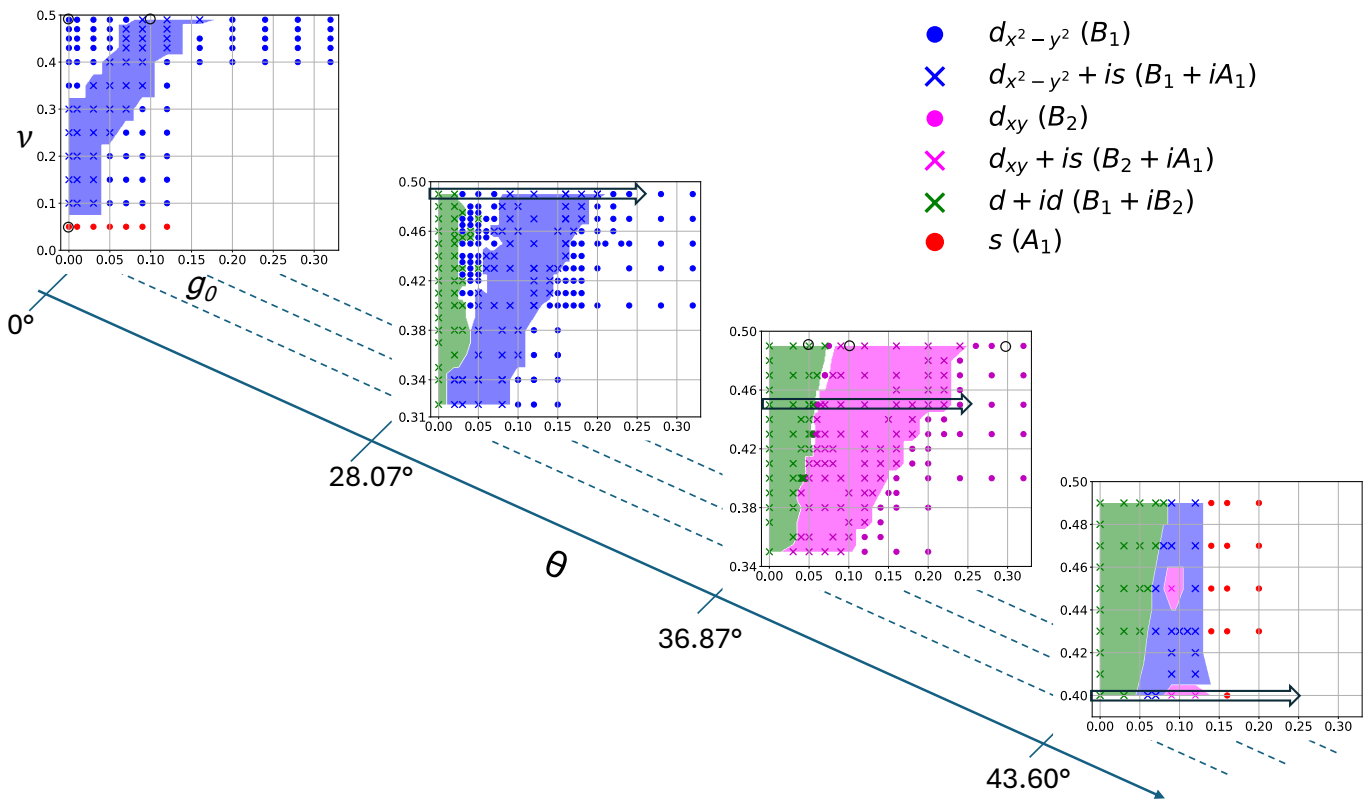


FIG. 9. Phase diagram for twisted bilayer cuprate as a function of twist angle (θ), filling (ν) and tunneling strength (g_0) for fixed interaction strength $V=0.2$. Each panel represents the phase diagram for a particular twist angle as a function of filling and tunneling strength. The blue dots represent TRS B_1 wave states, the blue crosses are for $B_1 + iA_1$ states and the blue regions mark the phase boundary for this state. Magenta dots are for B_2 states, magenta crosses represent the $B_2 + iA_1$ state with the magenta colored region being the phase boundary for this particular TRSB state. The $B_1 + iB_2$ state is represented by green crosses and the phase boundary by the green region. Finally, the pure s wave states are represented by red dots. The black circles in $\theta = 0$ and $\theta = 36.86$ represent the points in the phase diagram for which we have investigated the sublattice spectral functions and Fermi surface in Fig. 10. The arrows in the phase diagram of $\theta = 28.08^\circ$, $\theta = 36.87^\circ$ and $\theta = 43.60^\circ$ are the regions for which we have examined the evolution of each irrep in Fig. A4.

at $\theta = 0^\circ$ by plotting in Fig. 11 the normal state DOS as a function of g_0 and ν . The solid lines in the figure represent DOS for $\nu = 0.49$ for various g_0 . Increasing g_0 leads to splitting of the Van Hove singularity and for a range of values it lies in proximity to the chemical potential coinciding with the observed TRSB $B_1 + iA_1$ states, eventually moving away. For $\nu = 0.49$, the range is $g_0 \approx [0.07, 0.16]$. The insert in Fig. 11 displays the shift of the Van Hove singularity as we change filling. We observe that for the same $g_0 = 0.05$ the Van Hove singularity for $\nu = 0.4$ is shifted right and hence closer to the chemical potential as compared to $\nu = 0.49$ indicating that we need a smaller g_0 to bring the Van Hove singularity close to the chemical potential as we move away from half filling. This explains why we observe TRSB at smaller g_0 as we decrease filling in Fig. 9.

To understand the different phases in our phase diagram we investigate the normal state sublattice spectral function, defined as diagonal components of the full spec-

tral function matrix

$$A_\alpha(\mathbf{k}, \omega) = -\frac{1}{\pi} \text{Im}[(\omega + i\eta)\mathbb{1} - H_0(\mathbf{k})]_{\alpha\alpha}^{-1}, \quad (6)$$

where H_0 is the non interacting part of the Hamiltonian as derived in Eq. (A6), $\mathbb{1}$ is an identity matrix and α is the Moiré site index. For the Fermi surface $\omega = 0$ and hence we examine $A_\alpha(\mathbf{k})$ to obtain some key insights about the evolution of the order parameter across the phase diagram. The presence of high spectral weight in the Fermi surface anti-nodal regions of a given order parameter symmetry favors the state by lowering the condensation energy. We first consider various cases for the untwisted bilayer $\theta = 0^\circ$ to understand the different phases. Fig. 10(a) is simply the Fermi surface for $\nu = 0.49$ and $g_0 = 0$, together with plots of the spectral functions of the two sites in the Moiré unit cell, identical in this case. The sheets at the M point have spectral weights near the antinodes of the B_1 order parameter, thus stabilizing this state as is well-known. Fig 10(b) is plotted for $\nu = 0.49$ and $g_0 = 0.1$, where the Fermi surface is already considerably more complicated, including a small

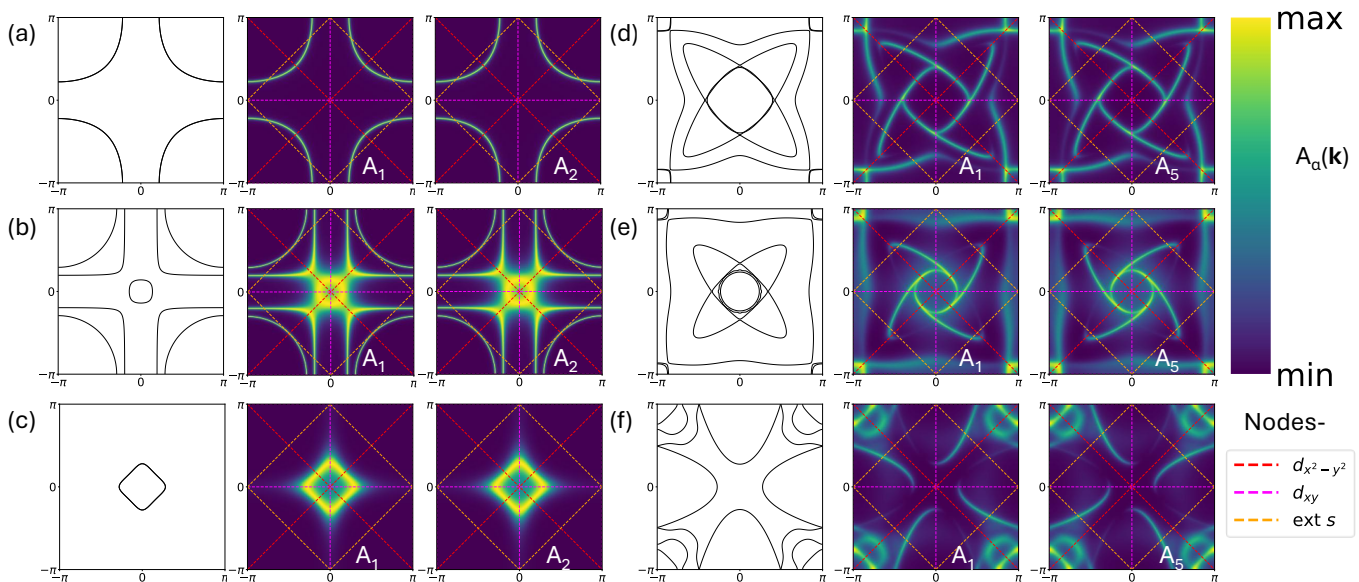


FIG. 10. Fermi surface and sublattice spectral function ($A_\alpha(\mathbf{k})$) for various parameters in the phase diagram. The overlap of the spectral function with the antinodes of an order parameter symmetry reduces the condensation energy hence favoring a particular state. The Γ point is located at $(0, 0)$ and the M points are located along the corners (π, π) , $(-\pi, \pi)$, $(\pi, -\pi)$ and $(-\pi, -\pi)$. The observed phases in the phase diagram can be understood by looking at the sublattice spectral functions for certain cases. (a) $\theta = 0^\circ$, $g_0 = 0$, $\nu = 0.49$, B_1 wave. (b) $\theta = 0^\circ$, $g_0 = 0.1$, $\nu = 0.49$, $B_1 + iA_1$ wave. (c) $\theta = 0^\circ$, $g_0 = 0$, $\nu = 0.05$, A_1 wave. (d) $\theta = 36.87^\circ$, $g_0 = 0.05$, $\nu = 0.49$, $B_1 + iB_2$ wave. (e) $\theta = 36.87^\circ$, $g_0 = 0.1$, $\nu = 0.49$, $B_2 + iA_1$. (f) $\theta = 36.87^\circ$, $g_0 = 0.3$, $\nu = 0.49$, B_2 wave.

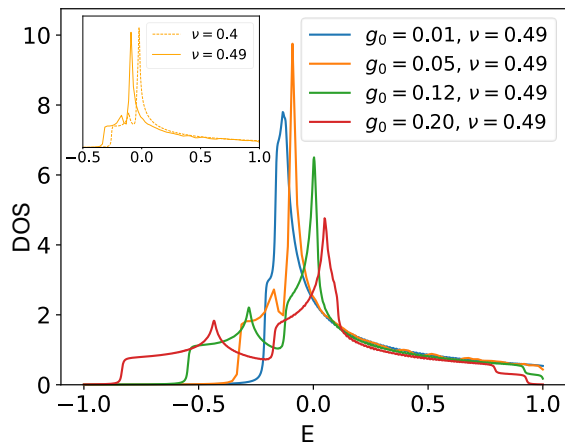


FIG. 11. Normal state DOS vs E for different g_0 for $\theta = 0$. The Van Hove singularity splits and shifts as we increase g_0 and we observe $B_1 + iA_1$ states in region where the Van Hove singularities lie in proximity of the chemical potential. The insert shows a shift of the Van Hove singularities closer to the chemical potential as we decrease filling for $g_0 = 0.05$.

pocket around Γ . As seen in the spectral function plots, the $B_1 + iA_1$ wave state is stabilized by the combination of spectral weight close to the M point and the Γ point in the normal state, i.e. regions near of the antinodes of B_1 and A_1 irrep. A simple confirmation is provided in Fig 10(c), plotted for small filling $\nu = 0.05$ and $g_0 = 0$ with only one pocket around the Γ point which stabi-

lizes A_1 wave (extended- s) state, the only state with an antinode there.

In Fig. 10(d)-(f), we now investigate similar features for $\theta = 36.87^\circ$ to obtain an idea about the transitions between the different phases at nontrivial twist. Fig. 10(d) shows the Fermi surface and sublattice spectral weight for $\nu = 0.49$ and $g_0 = 0.05$. The presence of significant $A_1(\mathbf{k})$ and $A_5(\mathbf{k})$ spectral weight in the antinodal region of B_1 and B_2 and its absence from antinodal regions of A_1 wave favors a $B_1 + iB_2$ state, as observed in Fig. 9. Fig. 10(e) is plotted for $\nu = 0.49$ and $g_0 = 0.1$ where the spectral function on the Γ pocket is much larger, thus leading to a $B_2 + iA_1$ state. Fig. 10(f) is for $\nu = 0.49$ and $g_0 = 0.3$ and the only regions with significant spectral weights lie along the antinodes of B_2 order parameter and thus this irrep is stabilized.

V. TEMPERATURE DEPENDENCE OF THE ORDER PARAMETER

The study of the phase diagram and its properties presented thus far have all been done at very low temperatures, where we have shown that multiple irreps compete with each other. At nonzero temperatures, all states corresponding to a given irrep must have the same critical temperature, but different irreps Γ will condense generally at different T_c^Γ . This means that a TRSB state will generally evolve into a TRS state with a single component as the temperature is raised.

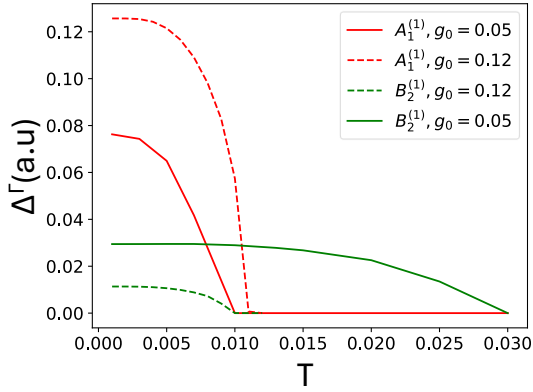


FIG. 12. Temperature dependence of different order parameter irreps for 53.13° twist for $g_0 = 0.05$ and $g_0 = 0.12$.

Without attempting to present a full phase diagram vs. T , we illustrate this phenomenon by examining the evolution of the different irreps of the order parameter Δ^Γ as a function of temperature. In Fig. 12 we choose two $B_2 + iA_1$ states for $\theta = 36.87^\circ$, $\nu = 0.4$ and $g_0 = 0.05, 0.12$ located on opposite sides of the phase boundary. For $g_0 = 0.05$ the A_1 wave vanishes first as we increase temperature and the B_2 wave persists upto highest temperature thus determining the T_c . For $g_0 = 0.12$ the A_1 wave persists up to a larger T_c whereas the B_2 wave irrep vanishes, showing that as a function of temperature either A_1 or B_1 wave is stable, depending on Hamiltonian parameters.

VI. JOSEPHSON CRITICAL CURRENT

One of the possible explanations for the apparently inconsistent observations of dramatically suppressed Josephson critical current (J_c) [4] and significant J_c [12] in twisted BSSCO systems at 45° twist angle could be different superconducting states being stabilized for the two experimental setups as established by the competing phases in the phase diagram. Understanding how J_c varies in these different states could provide us with some insights to the observed differences.

For a given set of model parameters we start with the fully converged order parameter; then, to calculate J_c we change the phase in one of the monolayers by ϕ which we then vary to plot a J vs ϕ curve, choosing the maximum value of J as J_c . The expression for the same is

$$J(\phi) = -\frac{ie}{\hbar} \sum_{(\alpha, \mathbf{u}), (\beta, \mathbf{v})\sigma} g_{\alpha\beta}^{\mathbf{u}\mathbf{v}} \langle c_{\alpha\sigma}^{\mathbf{u}\dagger} c_{\beta\sigma}^{\mathbf{v}} - c_{\beta\sigma}^{\mathbf{v}\dagger} c_{\alpha\sigma}^{\mathbf{u}} \rangle_\phi, \quad (7)$$

where sites $(\alpha, \mathbf{u}), (\beta, \mathbf{v})$ belong to different monolayers and $\langle c_{\alpha\sigma}^{\mathbf{u}\dagger} c_{\beta\sigma}^{\mathbf{v}} - c_{\beta\sigma}^{\mathbf{v}\dagger} c_{\alpha\sigma}^{\mathbf{u}} \rangle_\phi$ is obtained after solving the Hamiltonian with the phase changed order parameter to obtain the new creation and annihilation operators in

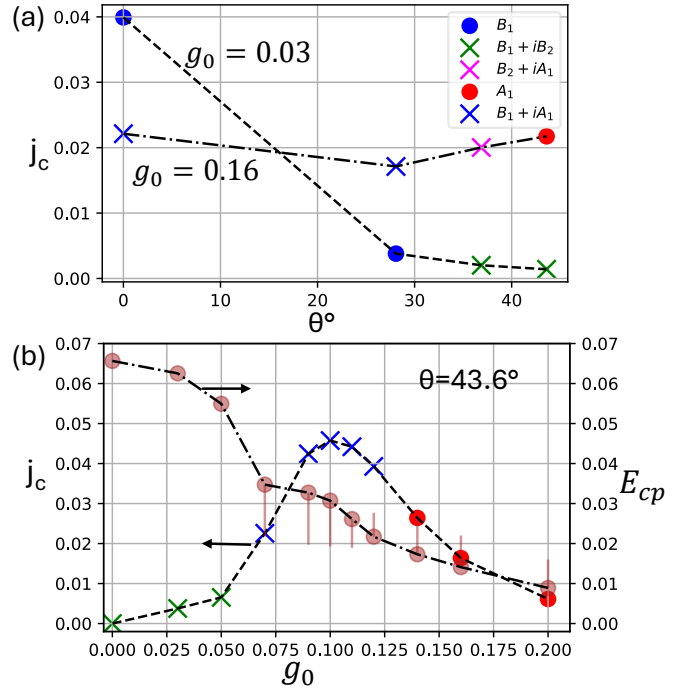


FIG. 13. Normalized Josephson critical current $j_c = (J_c \hbar a^2)/(e g_0 A)$ as the normalized Josephson critical current dependence on Hamiltonian parameters. (a) j_c vs θ for $\nu = 0.49$, $g_0 = 0.03$ and $\nu = 0.49$, $g_0 = 0.16$. (b) j_c vs g_0 and E_{cp} vs g_0 for $\nu = 0.43$ and $\theta = 43.6^\circ$. The brown circles are estimate for coherence peak energies (E_{cp}). Some values have an error bar because the coherence peaks are not easily decipherable due to the proximity of the Van Hove peak to the chemical potential. The arrows indicate the y-axis associated for each plot

terms of the quasiparticle states. We define the dimensionless quantity $j_c = (J_c \hbar a^2)/(e g_0 A)$ as the normalized J_c . In this definition, we have explicitly divided out the trivial g_0 scaling. A is the area of the Moiré unit cell for a commensurate twist angle θ . j_c is suitable to better understand the effect of the order parameter symmetry on the measured J_c . We note that for numerical reasons, the order parameter used in the calculation of Eq. (7) is not calculated self-consistently in the presence of the current, as has been also the case in previous calculations [14]. We believe this does not affect the qualitative results presented below.

As seen in Fig. 13(a), for a fixed $g_0 = 0.03$ and $\nu = 0.49$, j_c monotonically decreases by two orders of magnitude from $\theta = 0^\circ$ as θ increases to $\theta = 43.6^\circ$. This result is consistent with the experimental observation by Zhao et al [4] in twisted BSSCO crystals. For higher g_0 , we observe very little angle dependence of j_c , which is consistent with observations reported by Zhu et al. for twisted monolayers [12]. Thus the discrepancy between the two experiments could plausibly be explained by postulating that the essential difference between the two is a larger effective interlayer coupling in the latter. We speculate that this may be due to roughness of the surfaces

in the monolayer experiment, but there is no reported experimental evidence for this. Note that if this explanation is correct, it suggests that the monolayer system may realize completely different ground states than the anticipated $B_1 + iB_2$, to wit the TRSB $B_1 + iA_1$ or even TRS A_1 states.

To verify how competing order parameters change j_c for a fixed twist angle we plot j_c vs g_0 for $\theta = 43.6^\circ$, $\nu = 0.43$ in Fig 13(b). We observe that by increasing g_0 we move from a $B_1 + iB_2$ phase with very small j_c to a $B_1 + iA_1$ phase which is a TRSB state but with a larger j_c and finally to the TRS A_1 phase. We observe that j_c increases up to $g_0 = 0.10$ and then decreases.

To understand the dependence of the critical current on the tunneling energy g_0 , we plot in the same graph the coherence peak energies (E_{cp}) as a proxy for the overall magnitude of the superconducting order parameter. Note that in some cases the Van Hove peaks lie close to the chemical potential and the coherence peaks are not easily distinguishable, which we indicate with error bars for certain values of g_0 . We see a monotonic decrease of the order parameter magnitude as g_0 is increased, explaining the decrease of j_c in the large tunneling regime. We believe this is due to deviation from optimal conditions for d wave pairing as g_0 is increased. For $g_0 \rightarrow 0$, the order parameter saturates to its value in each isolated layer, while j_c decreases. This behavior can be explained from a perturbative argument how the expectation value $\langle c_{\alpha\sigma}^{u\dagger} c_{\beta\sigma}^v - c_{\beta\sigma}^{v\dagger} c_{\alpha\sigma}^u \rangle_\phi$ scales as a function of g_0 . For small g_0 , the self-consistently obtained order parameter and chemical potential are unaffected, so the onset of the expectation value comes from the scaling of the components of the eigenvectors. The BdG Hamiltonian acquires off-diagonal elements proportional to g_0 that couple arbitrary eigenstates with energy E_1 and E_2 . We now examine how the eigenvectors of the following 2×2 matrix scales with g_0 ,

$$\begin{bmatrix} E_1 & g_0 \\ g_0 & E_2 \end{bmatrix} = \frac{E_1 + E_2}{2} + \frac{E_1 - E_2}{2} \sigma_z + g_0 \sigma_x. \quad (8)$$

Calculating the unitary transformation that diagonalizes this matrix, we can express the c operators in the band basis to calculate the expectation value in Eq. (7). For small g_0 , we find that the components of the eigenvectors scale linearly with g_0 , and therefore so does the expectation value. Hence for small g_0 , $j_c \propto g_0$ since the magnitude of the order parameter stays roughly constant. As g_0 is increased, eventually the order parameter symmetry changes, making j_c depart from the linear dependence, reaching a maximum until it monotonically decreases for large g_0 .

VII. DISCUSSION

The phase diagram of the twisted bilayer cuprate provides us with insight into the nature of the TRSB state inferred from data in Ref. [4]. We observed that

the existence and nature of the TRSB state is sensitive to the magnitude of the tunneling and doping of the lattice model. We comment here on some possible numerical artifacts, and on how this model may be improved in the future.

Continuum model calculations[14, 15] also observe various types of TRSB states, which have been labeled in these works by their in-plane momentum dependence ($d + id$ or $d + is$). While these states are similar to the ones we also find, the notation used obscures somewhat their dependence on layer index which we have discussed in detail. To our knowledge, these works also did not explore the larger tunneling regime, where we find the fully gapped A_1 phase. However, they have done an extensive exploration of the effects of temperature on the TRSB states. Our spot checks of the T dependence of a few cases appears to agree qualitatively with the earlier work in parameter regimes where comparisons are possible. We performed our calculations starting with a random complex initial guess for the order parameter symmetry allowing for all irreps of the D_4 group as solutions whereas previous works have started with a $d + e^{i\phi} d'$ ansatz [1, 19].

The discrepancy in the experiments, Refs. [4] and [12], may be attributed to how the Josephson junctions were made. In Ref. [4], bulk BSSCO crystals were cleaved, twisted, and pressed together to form the junctions, whereas in Ref. [12] the BSSCO flakes were placed on a substrate. As mentioned in Ref. [12], there are variations in the tunnel barrier thickness due to local distortions. Zhu et al. [12] speculated that these distortions could allow for an s -wave component, but did not comment on a mechanism. We have pointed out here that enhanced tunneling will push the system locally towards an s wave component or even pure s ground state. Zhu et al. further note the possibility of a spontaneous breaking of the C_4 lattice symmetry by strain, potentially giving rise to an s -wave component. This effect may be more pronounced in thin flakes because fewer layers would offer less rigidity to shifts in positions of atoms in the unit cell. Finally, thin flakes are more susceptible to impurity effects which can lead to variations in the tunneling matrix elements[12]. It is evident from the above discussion that the tunneling form and strength play an important role in determining the order parameter symmetry. We believe that the most likely source of discrepancy between Refs. [4] and [12] is the induced change in electronic structure near points of low tunneling barriers, driving the system locally in to a state with an s wave component at 45° .

Since tunneling plays such an essential role in the phase diagram, it is important to perform a more precise treatment for the form of the tunneling matrix g_{ij} in a realistic model of a twisted BSSCO bilayer. This may be accomplished by numerically calculating overlaps of surface Wannier functions[23] at arbitrary twist angles. We will attempt a calculation of this type in future work.

VIII. CONCLUSIONS

To map out the phase diagram of twisted bilayer cuprates, in this work we studied a mean field model of two square lattices twisted to a relative commensurate angle, including in-layer nearest and next nearest hopping, nearest neighbor attraction and an interlayer tunneling term. We evaluated the superconducting gap function, a complicated function of Moiré coordinates, self consistently and determined the momentum and real space dependence.

The Moiré system formed by the commensurate twist of the two square lattices has a lower symmetry group D_4 as compared to the D_{4h} group for the isolated square lattices. Using the basis functions for each irrep, we determined the symmetry of the converged order parameter across our phase diagram. We also use properties of the real space order parameter to verify TRSB behavior of the order parameter. A thorough scan of the phase space as a function of twist angle, filling and doping demonstrates the presence of patches both TRSB and TRS states across the phase diagram. A study of the normal state DOS for $\theta = 0^\circ$ shows a strong correlation of the TRSB state with proximity of the Van Hove peaks to the chemical potential. Thus doping and tunneling strength influenced the ground state via the Van Hove position. However, we discussed also the role of the Fermi surface, which becomes more complex as the tunneling strength increases. We further exhibited the importance of the high spectral weight portions of the Fermi surface to the antinodal regions for the various competing states.

Finally, we calculated the Josephson critical current for various states. For small tunneling strength and filling near the Van Hove singularity, we reproduced the strong suppression of the critical current predicted by Can et al.[1] and measured by Zhao et al. [4] near 45° . However, the critical current at general nonzero twist remains significant for larger tunneling across a wide filling range in our calculations, because different TRSB states are dominant. At even larger tunneling, trivial A_1 states are induced that exhibit generic critical currents. We discussed the possibility that these differences could account for the roughly angle-independent critical current observed in the monolayer twist experiments of Zhu et al. [12]. Clearly it is essential to understand the microscopic nature tunneling matrix elements between the BSCCO layers to confirm the validity of this hypothesis.

ACKNOWLEDGMENTS

The authors are grateful to M. Franz and O. Can for discussions regarding their calculations, and to P. Volkov and J. Pixley for valuable discussions. We further thank Y. Wang for advice regarding the identification of TRSB states. S.P. and P.J.H. were partially supported by NSF-DMR-2231821. A.K. acknowledges support by

the Danish National Committee for Research Infrastructure (NUFI) through the ESS-Lighthouse Q-MAT.

Appendix A: Algorithm

The Hamiltonian for the twisted bilayer cuprate model is defined in Eq. (1). We need to redefine our Hamiltonian in the Moiré setup. Each site in our lattice is relabeled using two indices $i \rightarrow (\alpha, \mathbf{u})$ where α is the site index inside the Moiré unit cell and $\mathbf{u} = (u_x, u_y)$ is the Moiré unit cell coordinate. We also get rid of the layer index by labeling all the $2(m^2 + n^2)$ sites in our Moiré unit cell for a commensurate angle (m, n) as $0, 1, \dots, 2(m^2 + n^2)$ and since each monolayer has $m^2 + n^2$ sites if $\alpha \leq (m^2 + n^2)$ it belongs to first monolayer and if $(m^2 + n^2) < \alpha \leq 2(m^2 + n^2)$ then it belongs to the second monolayer.

We can understand the above notation using an example for $\theta = 53.13^\circ$. For this case $(m, n) = (1, 2)$ and the Moiré unit cell is shown in Fig. 1. The index runs from 1, ..., 10 where 1...5 marked with blue belong to the bottom monolayer and 6...10 marked with red belong to the top monolayer. In Fig. A1 we have neighboring Moiré unit cell for the bottom monolayer and the upspin creation operator corresponding to the sites marked by black circles are $c_{3\uparrow}^{(0,0)\dagger}$ and $c_{2\uparrow}^{(-1,-1)\dagger}$.

We rewrite the Hamiltonian in Eq. (1) in the Moiré setup

$$H = - \sum_{(\alpha, \mathbf{u}), (\beta, \mathbf{v}), \sigma} t_{\alpha\beta}^{\mathbf{uv}} c_{\alpha\sigma}^{\mathbf{u}\dagger} c_{\beta\sigma}^{\mathbf{v}} - \mu \sum_{(\alpha, \mathbf{u}), \sigma} n_{\alpha\sigma}^{\mathbf{u}} - \sum_{(\alpha, \mathbf{u}), (\beta, \mathbf{v})} V_{\alpha\beta}^{\mathbf{uv}} n_{\alpha}^{\mathbf{u}} n_{\beta}^{\mathbf{v}} - \sum_{(\alpha, \mathbf{u}), (\beta, \mathbf{v}) \sigma} g_{\alpha\beta}^{\mathbf{uv}} c_{\alpha\sigma}^{\mathbf{u}\dagger} c_{\beta\sigma}^{\mathbf{v}} \quad (\text{A1})$$

To evaluate the superconducting gap equation we first need to perform a mean field decomposition of Eq. (A1) resulting in

$$H = - \sum_{(\alpha, \mathbf{u}), (\beta, \mathbf{v}), \sigma} t_{\alpha\beta}^{\mathbf{uv}} c_{\alpha\sigma}^{\mathbf{u}\dagger} c_{\beta\sigma}^{\mathbf{v}} - \mu \sum_{(\alpha, \mathbf{u}), \sigma} n_{\alpha\sigma}^{\mathbf{u}} + \sum_{(\alpha, \mathbf{u}), (\beta, \mathbf{v})} \Delta_{\alpha\beta}^{\mathbf{uv}} c_{\alpha\uparrow}^{\mathbf{u}\dagger} c_{\beta\downarrow}^{\mathbf{v}\dagger} - \sum_{(\alpha, \mathbf{u}), (\beta, \mathbf{v}) \sigma} g_{\alpha\beta}^{\mathbf{uv}} c_{\alpha\sigma}^{\mathbf{u}\dagger} c_{\beta\sigma}^{\mathbf{v}}, \quad (\text{A2})$$

where

$$\Delta_{\alpha\beta}^{\mathbf{uv}} = V_{\alpha\beta}^{\mathbf{uv}} \langle c_{\alpha\uparrow}^{\mathbf{u}} c_{\beta\downarrow}^{\mathbf{v}} \rangle. \quad (\text{A3})$$

We solve our Hamiltonian in momentum space and hence we have to perform the Fourier transform of the above Hamiltonian where the annihilation operators in the Moiré setup transform as

$$c_{\alpha\uparrow}^{\mathbf{u}} = \sum_k c_{\mathbf{ak}\uparrow} e^{i\mathbf{k}\cdot\mathbf{u}}. \quad (\text{A4})$$

We make a list of all possible hopping, tunneling and interaction processes which are used to define the Hamiltonian. In the Moiré setup while considering any of the

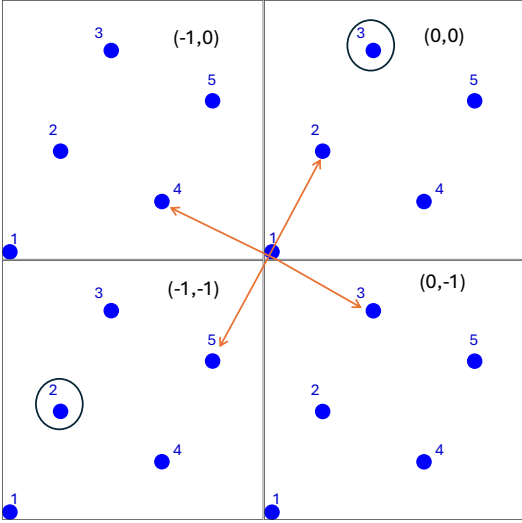


FIG. A1. Nearest neighbor hopping terms for site 1 for $\theta = 36.87^\circ$. We show the sites in one monolayer for the Moiré unit cells to which site 1 in unit cell $(0,0)$ can hop using the orange arrows. The Moiré unit cell coordinates are mentioned in the top right corner of each unit cell. Taking note of the site indices as well as the Moiré unit cell coordinates provides us with all the information required to solve the Hamiltonian Eq. (A2).

inter site hopping, tunneling or interaction terms of the Hamiltonian we need to store the information about the site indices as well as the Moiré unit cell coordinates as evident from Eq. (A2). We explain this using an example of 36.87° twist angle. Since hoppings are defined in a monolayer we show the Moiré unit cell with sites for one layer along with some of its neighboring cells which will be relevant in the further discussion in Fig. A1. The nearest neighbor hoppings from site 1 are shown in the figure. We can observe that the nearest neighbors for site 1 are site 2 in Moiré unit cell $(0,0)$, site 3 in Moiré unit cell $(0,-1)$, site 5 in Moiré unit cell $(-1,-1)$ and site 4 in Moiré unit cell $(-1,0)$.

An extensive list of all possible hoppings will contain this information for all the sites in our Moiré unit cell along with the hopping magnitude. We can generate similar list for next nearest neighbor hoppings as well as nearest neighbor interactions. The list of all possible tunneling terms can also be made similarly but the tunneling magnitude Eq. (2) changes for each i, j .

For any commensurate angle (m, n) we can rewrite the BdG Hamiltonian in Eq. (A2) using the Nambu vectors defined as $[c_{1k\uparrow}, \dots, c_{2(m^2+n^2)k\uparrow}, c_{1-k\downarrow}^\dagger, \dots, c_{2(m^2+n^2)-k\downarrow}^\dagger]^T$. The Moiré unit cell coordinate indices are not present here because they contribute in the Fourier transform as seen in Eq. (A4). The Hamiltonian in the matrix form is

$$H_{BdG}(\mathbf{k}) = \begin{bmatrix} H_0(\mathbf{k}) & \hat{\Delta}(\mathbf{k}) \\ \hat{\Delta}^\dagger(\mathbf{k}) & -H_0^T(-\mathbf{k}) \end{bmatrix}, \quad (\text{A5})$$

where $H_0(\mathbf{k})$ and $\hat{\Delta}(\mathbf{k})$ are $2(m^2+n^2) \times 2(m^2+n^2)$ matrices. $H_0(\mathbf{k})$ is the non-interacting part of the Hamiltonian consisting of hopping and tunneling terms whereas $\hat{\Delta}(\mathbf{k})$ contains the superconducting term of the Hamiltonian.

The structure of the non-interacting part of the Hamiltonian is as follows

$$H_0(\mathbf{k}) = \begin{bmatrix} H_{\text{hop},1}(\mathbf{k}) & H_{\text{tun},12}(\mathbf{k}) \\ H_{\text{tun},21}(\mathbf{k}) & H_{\text{hop},2}(\mathbf{k}) \end{bmatrix}, \quad (\text{A6})$$

where $H_{\text{hop},1}(\mathbf{k})$ and $H_{\text{hop},2}(\mathbf{k})$ are $(m^2+n^2) \times (m^2+n^2)$ matrices for the hopping terms in first and second monolayer respectively and $H_{\text{tun},12}$ and $H_{\text{tun},21}$ are also $(m^2+n^2) \times (m^2+n^2)$ matrices for the tunneling terms from layer $1 \rightarrow 2$ and $2 \rightarrow 1$ respectively.

We explicitly show the Fourier transform of the nearest neighbor hopping term in the Moiré setup to obtain the corresponding matrix element using our Nambu vectors. We have also used the fact that all our nearest neighbor hoppings have the same magnitude t .

$$\begin{aligned} & - \sum_{\langle(\alpha,\mathbf{u}),(\beta,\mathbf{v})\rangle\sigma} t_{\alpha\beta}^{\mathbf{u}\mathbf{v}} c_{\alpha\sigma}^{\mathbf{u}\uparrow} c_{\beta\sigma}^{\mathbf{v}} \\ & = -t \sum_{\langle(\alpha,\mathbf{u}),(\beta,\mathbf{v})\rangle\sigma\mathbf{k}\mathbf{k}'} c_{\alpha\mathbf{k}\sigma}^\dagger c_{\beta\mathbf{k}'\sigma} e^{-i\mathbf{k}\cdot\mathbf{u}+i\mathbf{k}'\cdot\mathbf{v}} \\ & = -t \sum_{\langle(\alpha,\mathbf{u}),(\beta,\mathbf{v})\rangle\sigma\mathbf{k}\mathbf{k}'} c_{\alpha\mathbf{k}\sigma}^\dagger c_{\beta\mathbf{k}'\sigma} e^{-i\mathbf{k}\cdot(\mathbf{u}-\mathbf{v})} \delta_{\mathbf{k}\mathbf{k}'} \\ & = -t \sum_{\langle(\alpha,\mathbf{u}),(\beta,\mathbf{v})\rangle\sigma\mathbf{k}} c_{\alpha\mathbf{k}\sigma}^\dagger c_{\beta\mathbf{k}\sigma} e^{-i\mathbf{k}\cdot(\mathbf{u}-\mathbf{v})}. \end{aligned} \quad (\text{A7})$$

The list of hopping and tunneling terms which we had discussed earlier in this section can then be used to find the correct Fourier factors between any such hopping term in $H_{\text{hop},1}(\mathbf{k})$ and $H_{\text{hop},2}(\mathbf{k})$. For example for $\theta = 36.87^\circ$ the nearest neighbor contribution for $H_{\text{hop},1}^{12}(\mathbf{k}) = -t$ since they both belong to the same Moiré unit cell but $H_{\text{hop},1}^{13}(\mathbf{k}) = -te^{-ik_y}$ since the hopping connects the two Moiré unit cells with coordinates $(0,0)$ and $(0,-1)$. We can find the contributions from the next nearest neighbor hopping and tunneling processes using the exact same method.

As mentioned earlier the superconducting part of the Hamiltonian $\hat{\Delta}(\mathbf{k})$ is also a $2(m^2+n^2) \times 2(m^2+n^2)$ matrix whose structure is greatly simplified because we only have interaction within each monolayer leading to offdiagonal elements being 0. The matrix is written as-

$$\hat{\Delta}(\mathbf{k}) = \begin{bmatrix} \hat{\Delta}_1(\mathbf{k}) & 0 \\ 0 & \hat{\Delta}_2(\mathbf{k}) \end{bmatrix}, \quad (\text{A8})$$

where $\hat{\Delta}_1(\mathbf{k})$ and $\hat{\Delta}_2(\mathbf{k})$ are $(m^2+n^2) \times (m^2+n^2)$ matrices, evaluated for monolayer 1 and 2 respectively using the list of interactions we have discussed above and Eq. (A3) after performing Fourier transform as shown in Eq. (A7). Since we only have nearest neighbor interactions we can rewrite

$$\Delta_{\alpha\beta}^{\mathbf{u}\mathbf{v}} = V \langle c_{\alpha\uparrow}^{\mathbf{u}} c_{\beta\downarrow}^{\mathbf{v}} \rangle, \quad (\text{A9})$$

where (α, \mathbf{u}) and (β, \mathbf{v}) are nearest neighbors. we define $\mathbf{r} = \mathbf{u} - \mathbf{v}$ and the Fourier transform is

$$\begin{aligned} \Delta_{\alpha\beta}(\mathbf{k}) &= \sum_{\mathbf{r}} V \langle c_{\alpha\uparrow}^{\mathbf{u}} c_{\beta\downarrow}^{\mathbf{v}} \rangle e^{-i\mathbf{k}\cdot\mathbf{r}} \\ &= \sum_{\mathbf{r}\mathbf{k}'} V \langle c_{\alpha\mathbf{k}'\uparrow} c_{\beta-\mathbf{k}'\downarrow} \rangle e^{-i(\mathbf{k}-\mathbf{k}')\cdot\mathbf{r}} \\ &= \sum_{\mathbf{k}'} V^{\mathbf{k}\mathbf{k}'} \langle c_{\alpha\mathbf{k}'\uparrow} c_{\beta-\mathbf{k}'\downarrow} \rangle, \end{aligned} \quad (\text{A10})$$

where

$$V^{\mathbf{k}\mathbf{k}'} = \sum_{\mathbf{r}} V e^{-i(\mathbf{k}-\mathbf{k}')\cdot\mathbf{r}}. \quad (\text{A11})$$

For a given twist angle and other Hamiltonian parameters, the calculation starts with defining a random complex initial guess for $\hat{\Delta}(\mathbf{k})$ for a defined momentum grid and evaluating the non-interacting part of the H_{BdG} Hamiltonian (Eq. (A5)) using the model parameters. We diagonalize H_{BdG} to obtain the quasiparticle eigenvalues and eigenvectors. The eigenvector matrix is inverted to obtain the creation and annihilation operators in our Nambu vectors in terms of the quasiparticle states. Using the creation and annihilation operators we calculate the filling $\nu = \sum_{\alpha\mathbf{k}\sigma} \langle c_{\alpha\mathbf{k}\sigma}^\dagger c_{\alpha\mathbf{k}\sigma} \rangle$ to evaluate the chemical potential self-consistently and also $\hat{\Delta}(\mathbf{k})$ which is then used as the input for the next iteration. The procedure is repeated till the order parameter converges to the desired precision.

Appendix B: The analytical form of the order parameter for $\theta = 90^\circ$

The 90° twist angle case is physically identical to the 0° twist case because of the C_4 symmetry of our twisted bilayer model. The difference between the two cases are in the Moiré unit cell since 0° has two sites, one per monolayer in the unit cell whereas 90° has 4 sites, 2 per monolayer. This difference leads to different momentum dependence of the order parameter in the two cases and also has a non-trivial imaginary part for 90° .

We can derive the analytic expression of the order parameter by starting with

$$H_{\Delta} = \sum_{(\alpha, \mathbf{u}), (\beta, \mathbf{v})} \Delta_{\alpha\beta}^{\mathbf{u}\mathbf{v}} c_{\alpha\uparrow}^{\mathbf{u}} c_{\beta\downarrow}^{\mathbf{v}} + h.c., \quad (\text{B1})$$

where H_{Δ} is the superconducting part of the Hamiltonian, $\Delta_{\alpha\beta}^{\mathbf{u}\mathbf{v}}$ is the order parameter between sites (α, \mathbf{u}) , (β, \mathbf{v}) .

We need to perform the Fourier transform of Eq. (B1) using the list of nearest neighbor interactions. We perform the calculation for $\Delta_{12}(\mathbf{k})$ term in the order parameter matrix as an example. Fig. A2 displays the nearest neighbors for site 1. The list includes site 2 belonging to Moiré unit cells with coordinates

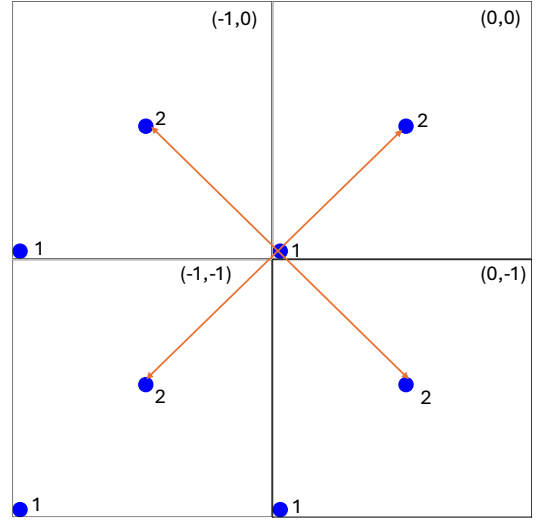


FIG. A2. Nearest neighbor hopping terms for site 1 for $\theta = 90^\circ$. We show the sites in one monolayer for the Moiré unit cells to which site 1 in unit cell $(0,0)$ can hop using the orange arrows. The Moiré unit cell coordinates are mentioned in the top right corner of each unit cell.

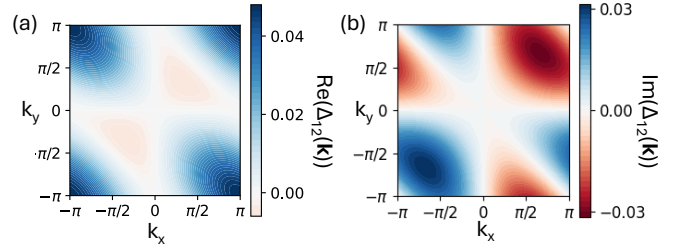


FIG. A3. Analytic calculation results for $\theta = 90^\circ$. (a) Real part of d wave order parameter. (b) Imaginary part of d wave order parameter. The from exactly matches the Δ_{12} form obtained in the numerical results in Fig. 4

$(0,0)$, $(0,-1)$, $(-1,0)$, $(-1,-1)$ in units of Moiré unit cell coordinate b .

Expanding Eq. (B1) for the above list of hoppings and performing the Fourier transform gives us

$$\begin{aligned} H_{\Delta_{12}} &= \sum_{\mathbf{k}, \mathbf{k}'} \Delta_{12}^{(0,0),(0,0)} c_{1\mathbf{k}\uparrow}^\dagger c_{2\mathbf{k}'\downarrow}^\dagger e^{-i\mathbf{k}\cdot(0,0)} e^{-i\mathbf{k}'\cdot(0,0)} \\ &+ \Delta_{12}^{(0,0),(0,-1)} c_{1\mathbf{k}\uparrow}^\dagger c_{2\mathbf{k}'\downarrow}^\dagger e^{-i\mathbf{k}\cdot(0,0)} e^{-i\mathbf{k}'\cdot(0,-1)} \\ &+ \Delta_{12}^{(0,0),(-1,-1)} c_{1\mathbf{k}\uparrow}^\dagger c_{2\mathbf{k}'\downarrow}^\dagger e^{-i\mathbf{k}\cdot(0,0)} e^{-i\mathbf{k}'\cdot(-1,-1)} \\ &+ \Delta_{12}^{(0,0),(-1,0)} c_{1\mathbf{k}\uparrow}^\dagger c_{2\mathbf{k}'\downarrow}^\dagger e^{-i\mathbf{k}\cdot(0,0)} e^{-i\mathbf{k}'\cdot(-1,0)} + h.c. \end{aligned} \quad (\text{B2})$$

For a d wave order parameter bonds at an angle 90° from each other have opposite signs and equal magnitude.

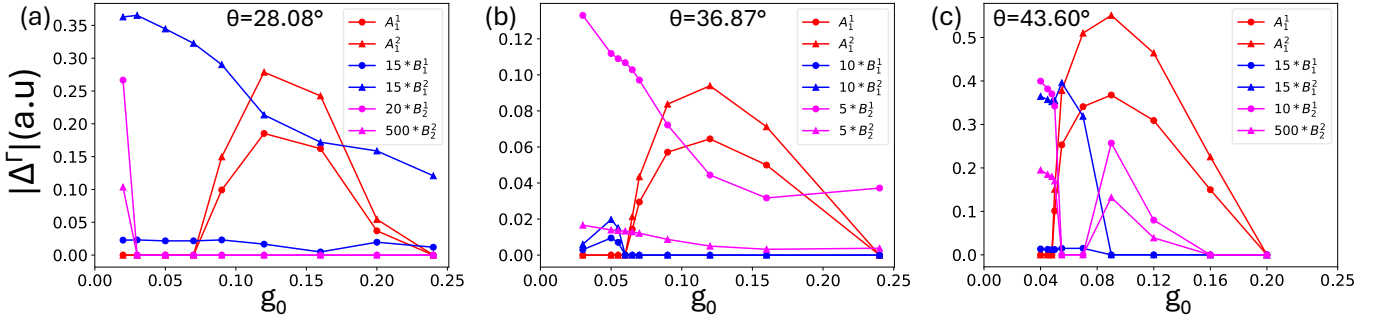


FIG. A4. $|\Delta^u|$ vs g_0 for various θ . (a) $\theta = 28.08^\circ$ and $\nu = 0.49$. (b) $\theta = 36.87^\circ$ and $\nu = 0.45$. (c) $\theta = 43.6^\circ$ and $\nu = 0.4$. The notation of the basis function in the plot legends has been provided in Table. I. For different θ we have different normalization factors for the irreps so that they lie on the same scale (see legend).

Using this property our equation is

$$\begin{aligned}
H_{\Delta_{12}} = & \sum_{\mathbf{k}, \mathbf{k}'} \Delta_{12} c_{1\mathbf{k}\uparrow}^\dagger c_{2\mathbf{k}'\downarrow}^\dagger e^{-i\mathbf{k}\cdot(0,0)} e^{-i\mathbf{k}'\cdot(0,0)} \\
& - \Delta_{12} c_{1\mathbf{k}\uparrow}^\dagger c_{2\mathbf{k}'\downarrow}^\dagger e^{-i\mathbf{k}\cdot(0,0)} e^{-i\mathbf{k}'\cdot(0,-1)} \\
& + \Delta_{12} c_{1\mathbf{k}\uparrow}^\dagger c_{2\mathbf{k}'\downarrow}^\dagger e^{-i\mathbf{k}\cdot(0,0)} e^{-i\mathbf{k}'\cdot(-1,-1)} \\
& - \Delta_{12} c_{1\mathbf{k}\uparrow}^\dagger c_{2\mathbf{k}'\downarrow}^\dagger e^{-i\mathbf{k}\cdot(0,0)} e^{-i\mathbf{k}'\cdot(-1,0)} + h.c.
\end{aligned} \tag{B3}$$

In the Cooper channel $\mathbf{k}' = -\mathbf{k}$ and hence we obtain.

$$\begin{aligned}
H_{\Delta_{12}} = & \sum_{\mathbf{k}} \Delta_{12} c_{1\mathbf{k}\uparrow}^\dagger c_{2-\mathbf{k}\downarrow}^\dagger \\
& - \Delta_{12} c_{1\mathbf{k}\uparrow}^\dagger c_{2-\mathbf{k}\downarrow}^\dagger e^{-ik_y} \\
& + \Delta_{12} c_{1\mathbf{k}\uparrow}^\dagger c_{2-\mathbf{k}\downarrow}^\dagger e^{-i(k_x+k_y)} \\
& - \Delta_{12} c_{1\mathbf{k}\uparrow}^\dagger c_{2-\mathbf{k}\downarrow}^\dagger e^{-ik_x} + h.c,
\end{aligned} \tag{B4}$$

and thus the Hamiltonian reduces to

$$\begin{aligned}
H_{\Delta_{12}}(\mathbf{k}) = & \Delta_{12} c_{1\mathbf{k}\uparrow}^\dagger c_{2-\mathbf{k}\downarrow}^\dagger (1 - e^{ik_y} + e^{i(k_x+k_y)} - e^{ik_x}) \\
& + h.c
\end{aligned} \tag{B5}$$

giving us an order parameter of the form

$$\begin{aligned}
\Delta_{12}(\mathbf{k}) = & \Delta_{12} [(1 + \cos(k_x + k_y) - \cos(k_x) - \cos(k_y)) \\
& + i(\sin(k_x + k_y) - \sin(k_y) - \sin(k_x))].
\end{aligned} \tag{B6}$$

which we plot in Fig. A3.

We can similarly find the order parameter form for the matrix elements of other twist angles (m, n) but it gets analytically challenging because the number of matrix elements in the order parameter matrix increase as we reach closer to 45° as m and n also increase

Appendix C: Order parameter evolution

The phase diagram in Fig. 9 displays the various states and transitions between them. To clearly observe these features we plot the non-normalized magnitudes of the order parameters ($|\Delta^u|$) in those phases, in Fig. A4. We project the converged order parameter onto different irreps basis functions and examine its evolution vs g_0 . The order parameter in these plots for different θ have been scaled differently for visual clarity (see legend). For $\theta = 28.08^\circ$ and $\nu = 0.49$ Fig. A4(a) shows that the B_1 order parameter is present throughout, whereas the B_2 order parameter is non-zero yet smaller than the B_1 state until it reaches 0 for $g_0 = 0.03$ indicating a $B_1 + iB_2$ state for small g_0 . Between $g_0 \approx [0.03, 0.07]$ a B_1 wave state is observed, and the A_1 order parameter with a larger magnitude coexists with the B_1 wave state for $g_0 \approx [0.07, 0.24]$, indicating a $B_1 + iA_1$ state. For $\theta = 36.87^\circ$ and $\nu = 0.45$ Fig. A4(b) shows a B_2 order parameter persisting throughout, whereas the B_1 order parameter is small and vanishes at $g_0 = 0.06$ and the A_1 order parameter then persists from $g_0 \approx [0.06, 0.24]$ and is the largest component of the order parameter for almost the whole range. For $\theta = 43.6^\circ$ and $\nu = 0.4$ shown in Fig. A4(c) we observe B_1 , B_2 and A_1 having non-zero values for $g_0 = 0.05$ indicating the coexistence region. Unique features of this twist angle include the existence of the gapped TRS A_1 state for large g_0 and the switching of the order parameter from B_1 to B_2 symmetry for $g_0 = 0.07$ but this is not a universal feature for all ν . For $g_0 > 0.2$ superconductivity is not stabilized in this parameter regime. For some of the twist angles in Fig. A4 we observe an order of magnitude difference between the scaling factors of two irreps but since the order parameter projections are not normalized for all possible basis functions we cannot make physical predictions.

[1] O. Can, T. Tummuru, R. P. Day, I. Elfimov, A. Damascelli, and M. Franz, High-temperature topological super-

conductivity in twisted double-layer copper oxides, Nature Physics **17**, 519 (2021).

- [2] K. Kuboki and M. Sigrist, Proximity-induced time-reversal symmetry breaking at Josephson junctions between unconventional superconductors, *Journal of the Physical Society of Japan* **65**, 361 (1996).
- [3] K. Kuboki and M. Sigrist, Time-reversal symmetry breaking surface states in t - J model, *Journal of the Physical Society of Japan* **67**, 2873 (1998).
- [4] S. Y. F. Zhao, X. Cui, P. A. Volkov, H. Yoo, S. Lee, J. A. Gardener, A. J. Akey, R. Engelke, Y. Ronen, R. Zhong, G. Gu, S. Plugge, T. Tummuru, M. Kim, M. Franz, J. H. Pixley, N. Poccia, and P. Kim, Time-reversal symmetry breaking superconductivity between twisted cuprate superconductors, *Science* **382**, 1422 (2023).
- [5] Q. Li, Y. N. Tsay, M. Suenaga, R. A. Klemm, G. D. Gu, and N. Koshizuka, $\text{Bi}_2\text{Sr}_2\text{CaCu}_2\text{O}_{8+\delta}$ bicrystal c -axis twist Josephson junctions: A new phase-sensitive test of order parameter symmetry, *Phys. Rev. Lett.* **83**, 4160 (1999).
- [6] Y. Takano, T. Hatano, A. Fukuyo, A. Ishii, M. Ohmori, S. Arisawa, K. Togano, and M. Tachiki, d -like symmetry of the order parameter and intrinsic Josephson effects in $\text{Bi}_2\text{Sr}_2\text{CaCu}_2\text{O}_{8+\delta}$ cross-whisker junctions, *Phys. Rev. B* **65**, 140513 (2002).
- [7] Y. I. Latyshev, A. P. Orlov, A. M. Nikitina, P. Monceau, and R. A. Klemm, c -axis transport in naturally grown $\text{Bi}_2\text{Sr}_2\text{CaCu}_2\text{O}_{8+\delta}$ cross-whisker junctions, *Phys. Rev. B* **70**, 094517 (2004).
- [8] J. Lee, W. Lee, G.-Y. Kim, Y.-B. Choi, J. Park, S. Jang, G. Gu, S.-Y. Choi, G. Y. Cho, G.-H. Lee, and H.-J. Lee, Twisted van der Waals Josephson junction based on a high- T_c superconductor, *Nano Letters* **21**, 10469 (2021), pMID: 34881903.
- [9] T. Confalone, F. Lo Sardo, D. Montemurro, D. Massarotti, V. M. Vinokur, G. Gu, F. Tafuri, K. Nielsch, G. Haider, and N. Poccia, Preserving the Josephson coupling of twisted cuprate junctions via tailored silicon nitride circuits boards, *Small* **21**, e06520 (2025).
- [10] A. C. Yuan, Y. Vituri, E. Berg, B. Spivak, and S. A. Kivelson, Inhomogeneity-induced time-reversal symmetry breaking in cuprate twist junctions, *Phys. Rev. B* **108**, L100505 (2023).
- [11] Y. Zhu, H. Wang, D. Zhang, and Q.-K. Xue, Manipulating fractional Shapiro steps in twisted cuprate Josephson junctions (2025), arXiv:2512.01586 [cond-mat.supr-con].
- [12] Y. Zhu, M. Liao, Q. Zhang, H.-Y. Xie, F. Meng, Y. Liu, Z. Bai, S. Ji, J. Zhang, K. Jiang, R. Zhong, J. Schneeloch, G. Gu, L. Gu, X. Ma, D. Zhang, and Q.-K. Xue, Presence of s -wave pairing in Josephson junctions made of twisted ultrathin $\text{Bi}_2\text{Sr}_2\text{CaCu}_2\text{O}_{8+\delta}$ flakes, *Phys. Rev. X* **11**, 031011 (2021).
- [13] H. Wang, Y. Zhu, Z. Bai, Z. Wang, S. Hu, H.-Y. Xie, X. Hu, J. Cui, M. Huang, J. Chen, Y. Ding, L. Zhao, X. Li, Q. Zhang, L. Gu, X. J. Zhou, J. Zhu, D. Zhang, and Q.-K. Xue, Prominent Josephson tunneling between twisted single copper oxide planes of $\text{Bi}_2\text{Sr}_2\text{CaCu}_2\text{O}_{8+\delta}$, *Nature Communications* **14**, 5201 (2023).
- [14] T. Tummuru, S. Plugge, and M. Franz, Josephson effects in twisted cuprate bilayers, *Phys. Rev. B* **105**, 064501 (2022).
- [15] J. H. Pixley and P. A. Volkov, Twisted nodal superconductors (2025), arXiv:2503.23683 [cond-mat.supr-con].
- [16] X.-Y. Song, Y.-H. Zhang, and A. Vishwanath, Doping a moiré Mott insulator: A $t - J$ model study of twisted cuprates, *Phys. Rev. B* **105**, L201102 (2022).
- [17] T. Y. Xie, W. Zhu, and J.-X. Zhu, Impurity effects on local electronic structure of twisted bilayer cuprates, *Phys. Rev. B* **110**, 134514 (2024).
- [18] O. Can, X.-X. Zhang, C. Kallin, and M. Franz, Probing time reversal symmetry breaking topological superconductivity in twisted double layer copper oxides with polar Kerr effect, *Phys. Rev. Lett.* **127**, 157001 (2021).
- [19] M. Fidrysiak, B. Rzeszutarski, and J. Spałek, Tuning topological superconductivity within the $t - J - U$ model of twisted bilayer cuprates, *Phys. Rev. B* **108**, 224509 (2023).
- [20] T. A. Maier and D. J. Scalapino, Pair structure and the pairing interaction in a bilayer Hubbard model for unconventional superconductivity, *Phys. Rev. B* **84**, 180513 (2011).
- [21] K. A. Musaelian, J. Betouras, A. V. Chubukov, and R. Joynt, Mixed-symmetry superconductivity in two-dimensional Fermi liquids, *Phys. Rev. B* **53**, 3598 (1996).
- [22] C. N. Breið, P. J. Hirschfeld, and B. M. Andersen, Superconductivity and spontaneous time-reversal symmetry breaking by nonmagnetic disorder in unconventional superconductors, *Phys. Rev. B* **105**, 014504 (2022).
- [23] A. Kreisel, P. Choubey, T. Berlijn, W. Ku, B. M. Andersen, and P. J. Hirschfeld, Interpretation of scanning tunneling quasiparticle interference and impurity states in cuprates, *Phys. Rev. Lett.* **114**, 217002 (2015).